5.7 A MEMS Coriolis Mass Flow Sensor with 300 µ g/h/√Hz Resolution and ± 0.8mg/h Zero Stability

De Oliveira, Arthur C.; Groenesteijn, Jarno; Wiegerink, Remco J.; Makinwa, Kofi A.A.

DOI
10.1109/ISSCC42613.2021.9365946

Publication date
2021

Document Version
Final published version

Published in
2021 IEEE International Solid-State Circuits Conference, ISSCC 2021 - Digest of Technical Papers

5.7 A MEMS Coriolis Mass Flow Sensor with 300µg/h/√Hz Resolution and ±0.8mg/h Zero Stability

Arthur C. de Oliveira[1], Jarno Groenesteijn[2], Remco J. Wiegerink[3], Kofi A. A. Makinwa[1]

[1]Delft University of Technology, Delft, The Netherlands
[2]Bronkhorst BV, Ruurlo, The Netherlands
[3]University of Twente, Enschede, The Netherlands

2021 IEEE International Solid- State Circuits Conference (ISSCC) | 978-1-7281-9549-0/20/$31.00 ©2021 IEEE | DOI: 10.1109/ISSCC42613.2021.9365946

Precision flow sensors are widely used in the pharmaceutical, food, and semiconductor industries to measure small amounts (<1gram/hour) of liquids and gases. MEMS thermal flow sensors currently achieve state-of-the-art performance in terms of resolution, size, and power consumption [1,3]. However, they only measure volumetric flow, and so must be calibrated for use with specific liquids [1] or gases [2,3]. In contrast, Coriolis flow sensors measure mass flow and thus do not need calibration for specific fluids. Furthermore, their resonance frequency can be used as a measure of fluid density. These features enable significant size, cost, and complexity reductions in low-flow microfluidic systems. Although much progress has been made, miniature [4] and MEMS [5-7] Coriolis mass flow sensors are still outperformed by their thermal counterparts, especially in terms of resolution and long-term stability.

This paper presents a dedicated CMOS interface for a MEMS Coriolis mass flow sensor. The sensor is fabricated using bulk-micromachining-based surface-channel technology to realize silicon-rich silicon nitride flow channels (<60µm diameter) [7]. Compared to sensors with silicon flow channels [5], higher mass flow sensitivity is achieved because the channel walls are quite thin (~1.2µm), making the mass of the flowing fluid larger than that of the channels. This also allows the sensor to be operated at atmospheric pressure. Compared to the state of the art [4-6], the overall flow-sensing system achieves significantly improved performance: 13× in resolution (300µg/h/√Hz), 12× in zero stability (±0.8mg/h), and 27× in power consumption, which puts it at par with state-of-the-art MEMS thermal flow sensors [1-3].

The operating principle of the MEMS Coriolis sensor is shown in Fig. 5.7.1. The suspended flow channel is driven into resonance around its drive axis (twist mode) at a frequency $\omega_T/2\pi$ (~1.78 to ~3kHz). The drive axis is excited by the Lorentz force created by an AC current (i_{DRIVE}) flowing through a metal track deposited on top of the channel in the presence of an external magnetic field (B). Mass flow (Φ) through the channel results in a Coriolis force perpendicular to the drive axis, thus exciting its sense axis (swing mode). This force is linearly proportional to mass flow. The displacement induced by the Lorentz and Coriolis forces is sensed by integrated comb capacitors $C_{D1,2}$ and $C_{S1,2}$, respectively (Fig. 5.7.1, bottom). In addition, a pick-up track, which runs beside the drive track, senses an induced electromotive force (ε), which is proportional to the channel's drive axis angular velocity.

To maintain the MEMS sensor in its linear operating region, the drive amplitude must be regulated. Although the comb capacitors enable low-noise readout of drive motion, the resulting current (I_T) will be modified by the physical properties of the fluid inside the channel, causing variations in the detected drive amplitude. A more robust alternative is to use the output of the pick-up track (ε) to regulate the drive angular velocity, and thus the generated Coriolis force. In this design, two complementary control loops are implemented: a low-noise drive loop based on the comb capacitors, which drives the sensor at its resonance frequency, and an amplitude-control loop based on the pick-up coil, which regulates the drive angular velocity.

Figure 5.7.2 shows a simplified block diagram of the system. It consists of three main parts: the MEMS sensor, the drive and amplitude-control loops, and the sense path. The drive loop uses HV-biased comb capacitors to sense drive motion. The resulting capacitance changes are converted to a voltage and then delayed by 90° to ensure oscillation. Finally, the sensor is driven by a variable-gain amplifier (VGA), whose gain is controlled by the amplitude-control loop. To suppress the amplitude-control $1/f$ noise and improve the sensor's long-term stability, the output of the pick-up coil is synchronously demodulated by mixing it with a phase-locked signal f_D obtained from the drive loop. The result is then compared to a reference voltage that sets the target amplitude. Finally, the loop filter, $L(s)$, attenuates the resonance and chopping harmonics while stabilizing the amplitude control. The sense path uses an IQ demodulator to detect the Coriolis signal (sense axis). The ratio between the in-phase (I) and quadrature (Q) components, which represents the phase shift between the drive and sense signals, is used to measure the mass flow, while the PLL output frequency provides fluid density information.

A simplified circuit diagram of the flow sensor's readout interface is shown in Fig. 5.7.3. The front-end of the drive loop consists of a capacitive transimpedance amplifier (C-TIA) based on an integrator-differentiator topology. The C-TIA has a gain of 148dBΩ and 12fA/√Hz input-referred current noise. A wide-range VGA is realized by using linearized MOSFETs as voltage-dependent resistors. At start-up, i_{DRIVE} may be quite large (~10mA), and so the VGA has a Class-AB output stage to drive the sensor efficiently. The amplitude-control loop consists of a chopped capacitively-coupled 1st stage with a gain of 40dB that up-modulates and boosts the induced ε signal. Its output is then synchronously demodulated by the 2nd stage, with a gain of 26dB, effectively demodulating the $f_{CH}\pm f_D$ components to f_{CH}. The result is then compared to a chopped off-chip reference voltage (V_{REF}), demodulated, and then filtered to attenuate the f_D and f_{CH} harmonics. To minimize the phase and noise contribution of the biasing networks, the time constants $C_1{\cdot}R_B$ and $C_{F2}{\cdot}R_B$ must be well below f_D and f_{CH}, respectively. This is achieved by implementing the large feedback resistances (>5GΩ) as switched resistors. Finally, the f_{CH}, f_D, and f_{PULSE} signals are synthesized from the drive phase with the help of a charge-pump PLL (CP-PLL) with an integer-N divider (N=128), which is locked to the zero crossings of V_{INT}.

The proposed readout IC was realized in a 0.18µm CMOS process and occupies a 1.2mm² active area, while the MEMS sensor occupies 10.4mm² (Fig. 5.7.7). The readout IC draws 8.1mA from a 1.8V supply. The sensor is characterized by mounting it over a custom fluidic connector. Figure 5.7.4 (top) shows its measured output response from liquids (H_2O, IPA, H_2O+IPA) to gases (N_2, Ar, CO_2, He) for mass flows up to 5g/h at room temperature and stable input pressure (6bar for gases, and 2bar for liquids). The ratio between phase shift and resonance frequency of all fluids is normalized by its maximum value for H_2O, and the sensitivity of N_2 is calibrated to match that of H_2O at 2g/h. The resulting calibration coefficient is then used for all fluids. As shown in Fig. 5.7.4 (top right), the sensor's sensitivity remains relatively constant for different fluids. The sensor's long-term zero stability (ZS) is derived from the standard deviation under zero flow conditions when filled with N_2 and H_2O. Over a 1h interval, it achieves a ZS of ±0.8mg/h for H_2O in a 3Hz bandwidth with a 300µg/h/√Hz noise floor (Fig. 5.7.4, bottom).

The sensor's change in resonance frequency seen from the PLL output is shown in Fig. 5.7.5 (top), which corresponds to a sensitivity of -160Hz/(kg/m³) from He to H_2O. The long-term stability of the density output signal is shown in Fig. 5.7.5 (bottom). The chopper-stabilized amplitude-control loop reduces the Allan deviation by almost 2×, showing the effectiveness of the flicker-noise suppression scheme.

Figure 5.7.6 summarizes the performance of the proposed MEMS Coriolis mass flow sensor and compares it with state-of-the-art flow sensors. Compared to previous Coriolis mass flow sensing systems, it achieves >13× higher resolution, >12× lower zero stability, and >27× less power consumption. It also achieves similar performance to state-of-the-art MEMS thermal flow sensors while consuming comparable power. This makes the proposed MEMS Coriolis system a promising candidate to replace MEMS thermal sensors in applications where both wide mass flow range and high resolution are required.

Acknowledgement:
The authors would like to thank the Dutch technology foundation STW, Bronkhorst BV, and KROHNE Nederland BV for financial support. We would also like to thank L. Pakula, Z. Chang, and R. van Puffelen for their help with the design of the measurement setup.

References:

[1] Sensirion AG, SLG-0025 Liquid Flow Meter Datasheet, Mar. 2019.
[2] M. Ahmed et al., "Fully Integrated Bidirectional CMOS-MEMS Flow Sensor with Low Power Pulse Operation," *IEEE Sensors J.*, vol. 19, no. 9, pp. 3415-3424, May 2019.
[3] W. Xu et al., "An Integrated CMOS MEMS Gas Flow Sensor with Detection Limit Towards Micrometer per Second," *IEEE MEMS*, pp. 200-203, Jan. 2020.
[4] Bronkhorst BV, mini CORI-FLOW™ Series ML120 Coriolis Mass Flow Meter Datasheet, Nov. 2019.
[5] R. Smith et al., "A MEMS-Based Coriolis Mass Flow Sensor for Industrial Applications," *IEEE Trans. Industrial Electronics*, vol. 56, no. 4, pp. 1066-1071, Apr. 2009.
[6] A. C. de Oliveira et al., "A MEMS Coriolis Mass Flow Sensing System with Combined Drive and Sense Interface," *IEEE Sensors*, pp. 1-4, Oct. 2019.
[7] D. Alveringh et al., "Integrated Pressure Sensing Using Capacitive Coriolis Mass Flow Sensors," *IEEE JMEMS*, vol. 26, no. 3, pp. 653–661, June 2017.

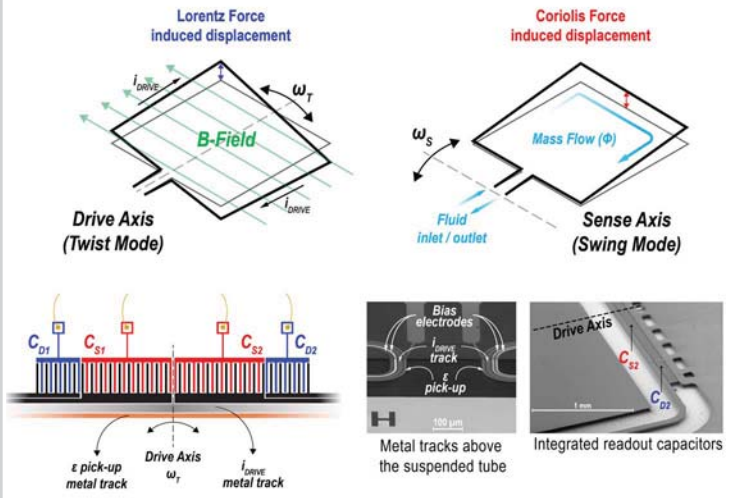

Figure 5.7.1: MEMS Coriolis mass flow sensor operating principle (top); readout capacitors, drive and induced pick-up metal tracks (bottom).

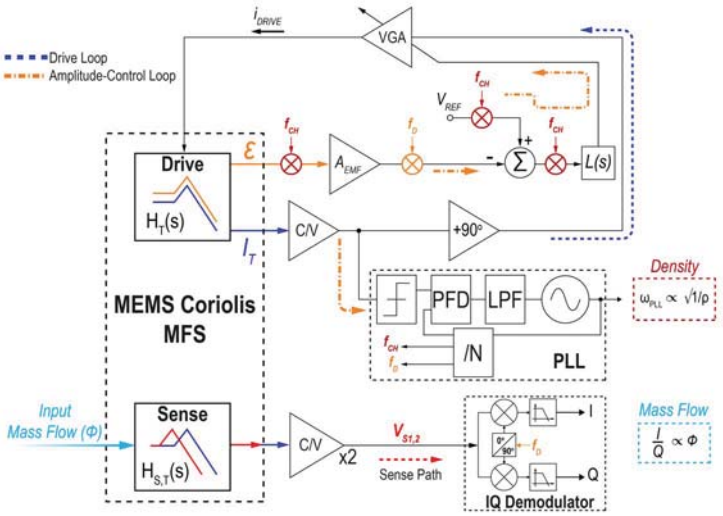

Figure 5.7.2: Simplified system block diagram.

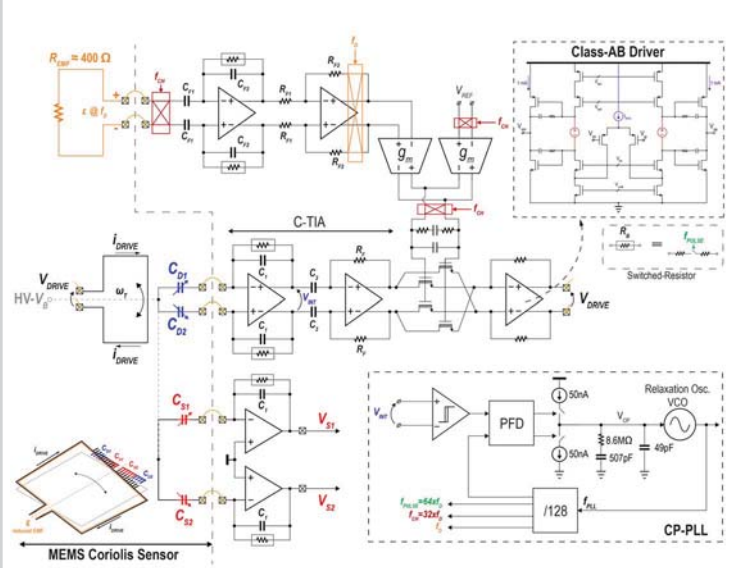

Figure 5.7.3: Circuit diagram of the proposed readout circuit.

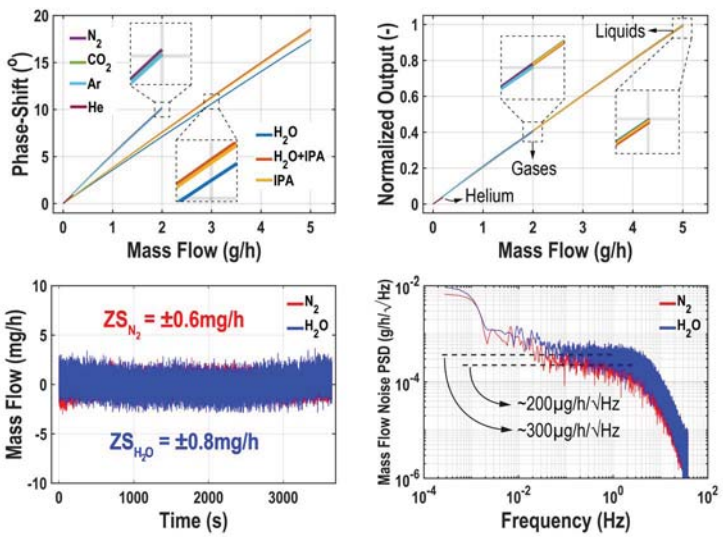

Figure 5.7.4: Measured sensor output response to mass flow (top left); and the normalized output calibrated at H_2O and N_2; zero stability (ZS) and noise floor from raw ADC data (bottom).

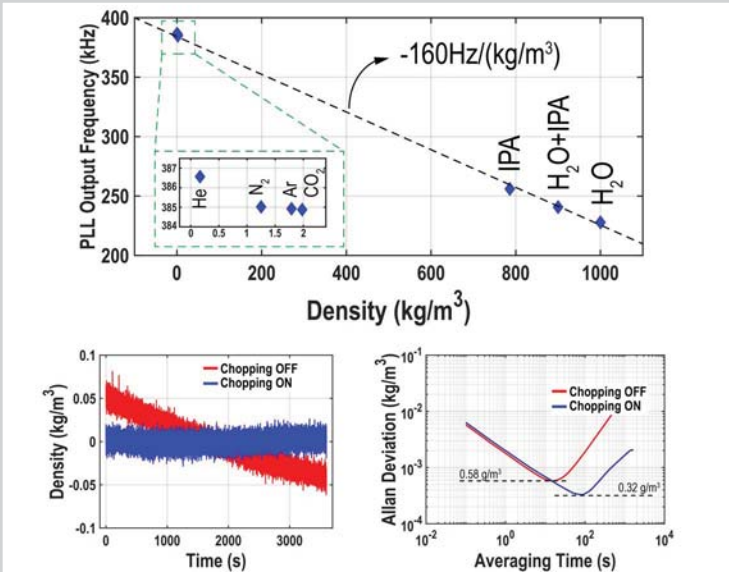

Figure 5.7.5: Measured change in resonance frequency for different fluids (top); density stability and Allan deviation when sensor is filled with N_2 (bottom).

	[1]	[2]	[3]	[4]	[5]	[6]	This Work	
Sensor Type	MEMS Thermal	MEMS Thermal	MEMS Thermal	Coriolis	MEMS Coriolis	MEMS Coriolis	MEMS Coriolis	
Readout Technology	CMOS	0.18µm CMOS	COTS	COTS	COTS	COTS	0.18µm CMOS	
Fluids	H_2O	N_2	N_2	Liquids & Gases	Liquids (H_2O)	N_2	Liquids & Gases	
Full Scale (g/h)	0.09	0.36[c]	0.6[c]	5	500	0.75	5	2
Resolution (mg/h/√Hz)	<0.6[a]	<0.2	<0.1	<4[a]	N/A	N/A	0.3	0.2
Bandwidth (Hz)	4	25	25	3	1.6	0.63	3	
Dynamic Range (dB)	39	51.1	61.6	60	N/A	N/A	79.5	71.5
Zero Stability (mg/h)	N/A	N/A	N/A	±10	±223	±2.6[b]	±0.8	±0.6
Power Consumption (mW)	21.5	8.9	13.1	2500	400	1250	14.6	

[a]Estimated from repeatability.
[b]1-sigma for a 80s measurement.
[c]Limited to the linear range.
N/A = Specification not available

Figure 5.7.6: Performance summary and comparison with previous works.

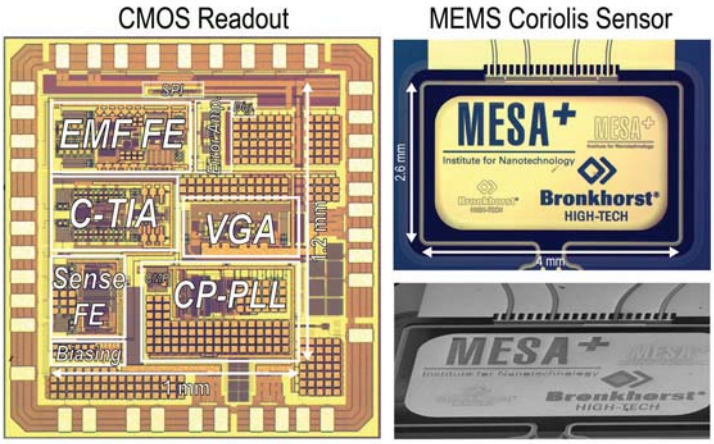

Figure 5.7.7: Micrograph of the CMOS die (left); MEMS micrograph and SEM image (right).

978-1-7281-9549-0/21/$31.00 ©2021 IEEE